# Harmonic-induced wave breaking due to abrupt depth transitions: an experimental and numerical study

S. Draycott[a,*], Y. Li[b,c], P. K. Stansby[a], T. A. A. Adcock[c], T. S. van den Bremer[c,d]

[a]*Department of Mechanical, Aerospace and Civil Engineering, University of Manchester, Manchester M60 1QD, UK*
[b]*Department of Energy and Process Engineering, Norwegian University of Science and Technology, N-7491 Trondheim, Norway*
[c]*Department of Engineering Science, University of Oxford, Parks Road, Oxford OX1 3PJ, UK*
[d]*Faculty of Civil Engineering and Geosciences, Delft University of Technology, Delft, 2628 CD, The Netherlands*

## Abstract

Abrupt depth transitions (ADTs) have been shown to induce the release of bound waves into free waves, which results in spatially inhomogeneous wave fields atop ADTs. Herein, we examine the role of free-wave release in the generation and spatial distribution of higher-harmonic wave components and in the onset of wave breaking for very steep periodic waves upon interaction with an ADT. We utilise a Smoothed Particle Hydrodynamics (SPH) model, making use of its ability to automatically capture breaking and overturning surfaces. We validate the model against experiments. The SPH model is found to accurately reproduce the phase-resolved harmonic components up to the sixth harmonic, particularly in the vicinity of the ADT. For the cases studied, we conclude that second-order free waves released at the ADT, and their interaction with the linear and second-order bound waves (beating), drive higher-order bound-wave components, which show spatial variation in amplitude as a result. For wave amplitudes smaller than the breaking threshold, this second-order beating phenomenon can be used to predict the locations where peak values of surface elevation are located, whilst also predicting the breaking location for wave amplitudes at the breaking threshold. Beyond this threshold, the contributions of the second-order and higher harmonics (second–harmonic amplitudes are up to 60% and sixth-harmonic up to 10% of the incident amplitude) cause breaking to occur nearer to the ADT, and hence the wave breaking onset location is confined to the region between the ADT and the first anti-node location of the second-order components. Counter-intuitively, we find that, at the point of breaking, steeper incident waves are found to display reduced non-linearity as a result of breaking nearer to the ADT.

*Keywords:* Smoothed Particle Hydrodynamics, Wave breaking, Non-linear waves, Abrupt depth transitions, Free-wave release, Harmonic analysis

*Corresponding author
*Email address:* samuel.draycott@manchester.ac.uk (S. Draycott)

## 1. Introduction

Abrupt depth transitions (ADTs) exist in the form of natural and man-made bathymetric features, such as seamounts, continental shelves, steep beaches, reefs, and breakwaters. The effect of variations in depth on the properties of surface waves in coastal waters has been the subject of an extensive literature (e.g., [1–7]). ADTs have been shown to release free waves [8, 9], transfer energy to higher frequencies [10–12], and, recently, induce rogue wave events [5, 13, 14]. Wave fields atop ADTs can be highly spatially variable and exhibit extreme crests, and as such have significant implications for the loading on structures placed on the shallower (or lee-) side of the ADT. This paper investigates the nonlinear behaviour of steep monochromatic waves atop ADTs with and without wave breaking.

For steep monochromatic waves in intermediate and uniform depth without breaking, wave nonlinearity is well understood. Most importantly, bound wave components are forced, which do not obey the (linear or nonlinear) dispersion relationship [15]. In the presence of an ADT, additional nonlinear phenomena occur, some of which have been explained by Massel [9] for weakly nonlinear monochromatic waves, up to second order in wave steepness. Waves are both transmitted and reflected by the ADT, and when the incident wave is weakly nonlinear, a release of bound waves into additional free waves at second order takes place. These free wave components do obey the linear dispersion relationship. The free superharmonic waves therefore travel at a phase speed different from the phase speed of the linear transmitted free waves (and their second-order superharmonic bound waves). This leads to a spatial beating pattern in the superharmonic surface elevation with a beating length of $\pi/(k_{2f_0,s} - 2k_{0,s})$, where $2k_{0,s}$ denotes the wavenumber of the transmitted second-order superharmonic bound wave and $k_{2f_0,s}$ the wavenumber of the second-order superharmonic free wave in the shallower depth. The first anti-node is observed at $\varphi_{2s}/(k_{2f_0,s} - 2k_{0,s})$, where $\varphi_{2s}$ denotes the phase shift between the superharmonic bound and free waves. For second-order waves in the limits of a small change in depth or very deep water on the deeper side $\varphi_{2s} = \pi$. This behaviour predicted by Massel [9] has been observed experimentally by Monsalve Gutiérrez [16].

By extending the theory of Massel [9] to narrow-banded wavepackets, Li et al. [17, 18] have demonstrated that beating of the second-order superharmonic waves only occurs within a limited distance from the top of the ADTs for non-monochromatic waves and that, in addition, second-order subharmonic free waves are generated. Based on the deterministic model developed by Li et al. [17], Li et al. [19] have proposed a mechanism for the formation of rogue waves atop ADTs by developing a second-order stochastic model. This model can explain the non-homogeneous statistical properties of irregular waves (e.g., skewness, kurtosis) atop ADTs observed in numerical simulations [5, 20–23] and experiments [13, 14, 23, 24].

Experiments and numerical simulations have also been used to examine the behaviour of steep monochromatic waves propagating over ADTs, including effects up to third order. In Ohyama and Nadaoka [25], a boundary element code is used to study nonlinear wave transformation over a submerged shelf, where significant third-order wave components are observed in addition to those at second order. Using a Boussinesq-type model for the shallower side, Grue [26] concluded that the second and third harmonic waves on the lee-side of an obstacle can, in some cases, be comparable to the amplitude of the incoming first harmonic.

Several experimental studies have demonstrated that higher-harmonic generation occurs as waves propagate over various types of depth transitions (both finite-length and stepped). The generation of higher harmonics were noticed on the lee-side of submerged breakwaters whose crests are near to the free surface in Dattatri et al. [27]. In Kojima et al. [11], a similar phenomenon is observed for finite and infinite length submerged plates, concluding that energy is transferred to higher frequencies. Highly irregular wave forms are observed after the depth increase for the finite-length plate case. This phenomenon is described as 'harmonic de-coupling' in Beji and Battjes [12], which occurs when waves propagate over the downward slope of a submerged bar. For the cases presented they conclude that this phenomenon is more dominant than wave breaking in terms of the redistribution of energy. In a subsequent numerical study by Beji and Battjes [28], a Boussinesq model was developed and found to accurately describe the wave transformations observed in [12]. These experimental and numerical studies support findings from early field work by Byrne [8], where additional wave components were observed due to shallow-water wave interaction with a natural submerged offshore bar. Similar findings were found in another field study by Young [10] assessing wave propagation over coral reefs.

It is clear from the aforementioned studies that second and third-harmonic components of the wave field can be significantly amplified when monochromatic waves travel over an ADT and that, separately, ADTs can be the cause of wave breaking. Through a comparison of new experiments and numerical simulations using Smoothed Particle Hydrodynamics (SPH) this paper will examine why steep monochromatic waves break atop ADTs and what the role of higher harmonics is in causing this breaking process and setting the breaking location.

In order to model steep waves interacting with varying bathymetry, numerical solvers that provide direct numerical solutions of the fully nonlinear potential flow (FNPF) equations can be used. However, such models are incapable of fully capturing wave breaking due to the potential flow assumption, which is violated in breaking waves. In FNPF models, waves are modelled as either a single-valued free surface or as a Lagrangian free surface, modelling the overturning jet to the point of re-connection with the surface below. A spilling-breaker model was successfully incorporated into a FNPF code in Grilli et al. [29] to prevent overturning and used to predict wave shoaling over mild slopes. However, to model the complete breaking process, computational fluid dynamics (CFDs) codes are required to solve the full Navier–Stokes equations. In Chella et al. [30], the incompressible Reynolds-averaged Navier–Stokes (RANS) are solved with a $k$-$\omega$ turbulence model to assess the breaking wave profile asymmetry over a submerged reef. They conclude that the water depth over the reef largely determines the wave breaking behaviour and breaker characteristics. A CFD study by Srineash and Murali [31] showed an increase in higher-harmonic content with increasing steepness as waves propagate over a mild-slope ramp. No breaking cases were carried out in [31].

In conventional Eulerian grid-based CFD models, maintaining mass conservation with overturning free surfaces is problematic, and alternative Lagrangian-particle approaches are increasingly used. The Lagrangian Smoothed Particle Hydrodynamics (SPH) framework is one such method, offering major advantages to modelling these free-surface flows (e.g., [32]). There are essentially two main variants of SPH: the weakly compressible form where fluid pressure and density are explicitly related through the Tait equation of state (Eq. (7)), and the incompressible form which maintains a divergence-free velocity field through the projection method (e.g., [33]).

Due to pressure noise resulting from the stiff equation of state, and the numerical diffusion techniques employed to resolve this (e.g., $\delta$-SPH, [34]), weakly-compressible SPH is known to suffer from non-physical pressure noise and excessive dissipation [35]. In contrast, the incompressible form of SPH has higher accuracy and better conservation properties (see e.g., [36]), but at greater computational expense. Recent advances in weakly compressible ($\delta$)-SPH have, however, demonstrated notable improvements in field quantities, energy and volume conservation, and in the reduction of non-physical dissipation [35]. In this paper we use the weakly compressible SPH code DualSPHysics [37, 38] with a more standard $\delta$-SPH scheme, described further in Section 2.2.

With particles of constant mass, the SPH approach models breaking without special treatment of the free surface (e.g., [39, 40]). SPH has also been used to model waves interacting with underwater obstacles. In Gotoh et al. [41] a SPH model with large-eddy simulation (see [42]) was used to model wave interaction with a partially submerged breakwater to assess turbulence and vortical flow. SPH has also been used to model shallow-water solitary waves interacting with a curtain-type breakwater in Shao [43], and Han and Dong [44] used SPH to assess shallow-water solitary waves interacting with a submerged breakwater, assessing breakwater performance and energy transmission coefficients. The performance of berm breakwaters after potential reshaping by storms was assessed using SPH in Akbari and Torabbeigi [45]. Additionally, the interaction of waves with submerged porous obstacles has been successfully modelled in Khayyer et al. [46] and Tsuruta et al. [47] using incompressible SPH models. None of these SPH-based studies focus on the ability of the model to capture the (higher-) harmonic waves and the resulting interaction on the shallower (or lee-) side of the ADT. This leads to the third objective of the paper: to validate SPH for the generation of higher harmonics, specifically due to an ADT. This will allow us to assess the nature and origin of the higher harmonics and their role in the onset of wave breaking.

The paper is laid out as follows. In Section 2, the experimental set-up and numerical method are described, and the test cases are defined. Section 2.4 presents a convergence study along with example outputs. Results are presented in Section 3, where in Section 3.1 and Section 3.2 a harmonic analysis is presented comparing between SPH simulations and experiments. Section 3.1 focuses on time and frequency-domain analysis, whilst Section 3.2 presents a spatial analysis of the transmitted superharmonics. Section 3.3 explores the role of the harmonics in determining the breaking onset and location. Concluding remarks are offered in Section 4.

## 2. Methodology

### *2.1. Experimental set-up*

Experiments were carried out in the COAST (Coastal, Ocean and Sediment Transport) laboratory at the University of Plymouth, UK. A false floor was installed in the 35 m long flume, which has a width of 0.6 m. The water depth, $h_d$, was set to 0.55 m, and the false floor installed with a height $h_{\text{step}} = 0.35$ m from 7.5 m to 22.5 m away from the wavemaker. Hence, the shallower side water depth, $h_s = h_d - h_{\text{step}} = 0.2$ m. A diagram of the test set-up is shown in Fig. 1, including the 12 resistance-type multiplexed wave gauges installed and used for analysis and model validation. All gauges are sampled at 128 Hz, and their positions are defined in Table 1.

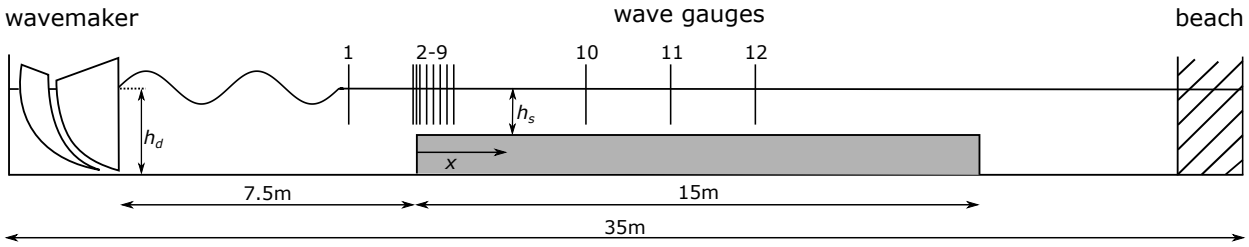


**Figure 1:** Diagram of experimental wave flume and set-up.

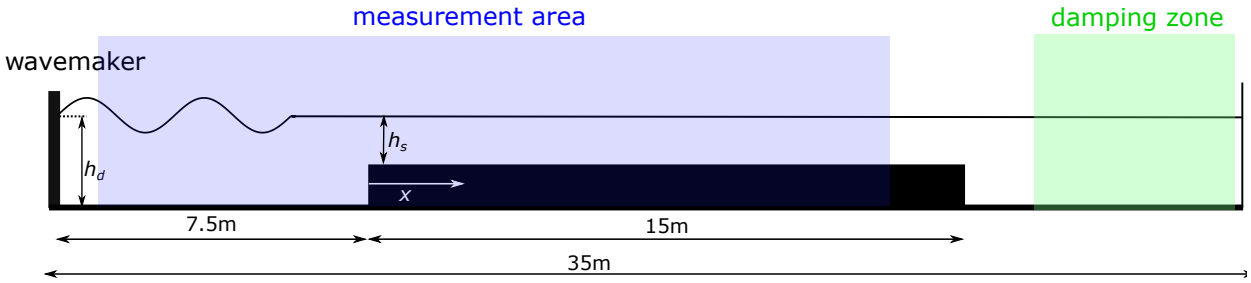


**Figure 2:** Diagram of numerical wave flume. Black regions denote solid boundaries.

| Gauge no. | 1 | 2 | 3 | 4 | 5 | 6 | 7 | 8 | 9 | 10 | 11 | 12 |
|---|---|---|---|---|---|---|---|---|---|---|---|---|
| Position [m] | -1.865 | -0.1 | 0 | 0.1 | 0.3 | 0.5 | 0.7 | 0.9 | 1.1 | 5 | 7.5 | 10 |

**Table 1:** Positions of the wave gauges relative to the depth transition ($x = 0$), as indicated in Fig. 1.

## 2.2. Numerical method

### 2.2.1. SPH implementation

The open-source code DualSPHysics [37, 38] is used for all SPH simulations, and both the fluid and solid domains are defined as discrete particles. The weakly-compressible form of the SPH equations are solved. In DualSPHysics, and SPH in general, the discrete approximation for a physical quantity, $\beta$, for particle $i$ is given by:

$$\beta_i = \sum_{j \in \Omega} \beta_j W_{i,j} V_j, \tag{1}$$

where $j \in \Omega$, and $\Omega$ is the set of neighbouring particles. The kernel function is denoted by $W_{i,j} = W(|\boldsymbol{x}_{i,j}|, h)$ and is calculated as a function of the distance between particles ($|\boldsymbol{x}_{i,j}| = |\boldsymbol{x}_i - \boldsymbol{x}_j|$) and the smoothing length, $h$. The volume of a neighbouring particle $j$ is denoted by $V_j$, and $V_j = m_j/\rho_i$ with $m_j$ and $\rho_j$ the mass and density of particle $j$, respectively.

For all simulations a quintic Wendland kernel [48] is used, defined as:

$$W_{i,j} = \alpha_D \, (1 - \frac{q}{2})^4 \, (2q + 1) \quad \text{for } 0 \leq q \leq 2, \tag{2}$$

where $q = |\boldsymbol{x}_{i,j}|/h$, and $\alpha_D$ is a normalisation term. For the 2D simulations presented in this paper $\alpha_D = 7/(4\,\pi h^2)$, and $h$ is set to $1.2\,\sqrt{2}\,d_p$, where $d_p$ is the particle spacing.

### 2.2.2. Governing equations

Fluid quantities are calculated based on the principles of conservation of mass (continuity) and momentum.:

$$\frac{\mathrm{D}\rho}{\mathrm{D}t} + \rho \nabla \cdot \mathbf{u} = 0, \tag{3}$$

$$\frac{\mathrm{D}\mathbf{u}}{\mathrm{D}t} = -\frac{1}{\rho}\nabla p + \mathbf{g} + \Gamma, \tag{4}$$

where $\rho$ is the fluid density, $\mathbf{u} = (u, v, w)$ is the velocity vector with components in the $(x, y, z)$-directions, $p$ is the fluid pressure, and $\mathbf{g}$ is gravitational acceleration. D/D$t$ denotes the material derivative and $\Gamma$ represents the dissipative terms.

The weakly-compressible SPH form of the continuity equation, including the $\delta$-SPH density diffusion term of [49], is given by:

$$\frac{\mathrm{d}\rho_\mathrm{i}}{\mathrm{dt}} = \sum_{j \in \Omega} m_j \boldsymbol{v}_{i,j} \cdot \boldsymbol{\nabla} W_{i,j} + \delta h c_0 \sum_{j \in \Omega} V_j \boldsymbol{\Psi}_{i,j} \cdot \boldsymbol{\nabla} W_{i,j}, \tag{5}$$

where $\boldsymbol{v}_{i,j} = \boldsymbol{v}_i - \boldsymbol{v}_j$ and $\boldsymbol{\nabla} W_{i,j}$ is the kernel gradient. The speed of sound $c_0$ is set to $20\sqrt{g h_d}$ for these simulations, where $\sqrt{g h_d}$ is the phase speed for a shallow-water wave in a water depth $h_d$. The acceleration due to gravity is denoted by g. The $\delta$-SPH coefficient, $\delta$, is taken to be the standard value of 0.1 (e.g. [50]). The diffusion term, $\boldsymbol{\Psi}_{i,j}$ is given by (as in [51]):

$$\boldsymbol{\Psi}_{i,j} = 2(\rho_j^D - \rho_i^D)\frac{\boldsymbol{x}_{i,j}}{|\boldsymbol{x}_{i,j}|} = 2(\rho_{i,j}^T - \rho_{i,j}^H)\frac{\boldsymbol{x}_{i,j}}{|\boldsymbol{x}_{i,j}|}, \tag{6}$$

which is the formulation first described in [49]. The superscripts $D, T$ and $H$ denote the dynamic, total and hydrostatic densities, respectively. For weakly-compressible SPH, the pressure and density, and hence conservation of mass and momentum equations, are coupled using the Tait equation of state:

$$p = \frac{c_0^2 \rho_0}{\gamma} \left[ \left( \frac{\rho}{\rho_0} \right)^{\gamma} - 1 \right], \tag{7}$$

where $\rho_0$ =1000 kg m$^{-3}$ is the reference density of water, and $\gamma = 7$ is the polytropic index. Eq. (7) is a very stiff equation, and coupled with particle disorder, results in significant non-physical density fluctuations. In our simulations, the aforementioned $\delta$-SPH density diffusion term in Eq. (5) is therefore introduced to reduce these density fluctuations.

The momentum equation, including artificial viscosity, is given by:

$$\frac{\mathrm{d}\boldsymbol{v}_\mathrm{i}}{\mathrm{dt}} = -\sum_{j \in \Omega} m_j \left( \frac{p_j + p_i}{\rho_i \rho_j} + \Pi_{i,j} \right) \boldsymbol{\nabla} W_{i,j} + \boldsymbol{g}, \tag{8}$$

where $\boldsymbol{g}$ is the gravitational acceleration vector, and $\Pi_{i,j}$ is the artificial viscosity term, which is defined as in [39], namely:

$$\Pi_{i,j} = \frac{-\alpha_\Pi c_0}{\rho_i + \rho_j} \frac{h \boldsymbol{v}_{i,j} \cdot \boldsymbol{x}_{i,j}}{|\boldsymbol{x}_{i,j}|^2 + 0.01 h^2}, \tag{9}$$

where $\alpha_\Pi$ is set to 0.01 (typically between 0.01 and 0.1).

Time-stepping is carried out using a symplectic explicit second-order time-integration method using a predictor and corrector stage. The Courant number is set to 0.2.

### *2.2.3. Numerical wave flume set-up*

The numerical wave flume is depicted in Fig. 2, and a summary of key parameters used for the simulations is provided in Table 2. The numerical flume is set up to have the same $x$ and $z$-dimensions as the physical flume depicted in Fig. 1. However, the numerical flume is a 2D model of the physical flume in order to obtain the high particle density required to capture wave breaking onset.

Based on preliminary validation studies, waves were simulated using a second-order wavemaker [53] without active wave absorption. To minimise reflected waves from the end of the computational domain, a large passively absorbing damping zone was defined from $x$ = 17.5 m to $x$ = 27 m (25 m to 34.5 m from the wavemaker). This damping zone reduces fluid velocities quadratically to zero over the length of the damping zone. A convergence study (Section 2.4) showed that a particle spacing $d_p$ = 0.005 m is sufficient for capturing the appropriate physics, particularly near to the depth transition. Surface elevation values were extracted every $d_p$ from -6.5 m to 12.5 m, enabling detailed spatial assessment of the wave fields. Velocities of SPH particles are also extracted over the same $x$-range to enable assessment and visualisation of breaking wave cases.

In order to provide improved estimates of fluid pressures near solid boundaries, all solid boundaries (tank walls, floor and wavemaker) are defined using the modified dynamic boundary conditions (mDBC) recently implemented in DualSPHysics [52].

| Parameter | Value |
|---|---|
| SPH Kernel | Quintic Wendland |
| Particle spacing ($d_p$) | 0.005 m |
| Smoothing length ($h$) | $1.2\sqrt{2}\,d_p$ |
| Density diffusion ($\delta$) | 0.1 |
| Diffusion term ($\mathbf{\Psi}_{i,j}$) | Fourtakas et al. [49] |
| Particle shifting | Off |
| Speed of sound ($c_0$) | $20\sqrt{gh_d}$ |
| Reference density ($\rho_0$) | 1000 kgm$^{-3}$ |
| Polytropic index ($\gamma$) | 7 |
| Artificial viscosity ($\alpha_\Pi$) | 0.01 |
| Time integration | Predictor-corrector |
| Courant number | 0.2 |
| Simulation time | 30 s |
| Simulation output frequency | 20 Hz |
| Dynamic boundary condition | mDBC [52] |

**Table 2:** Key parameters and formulations used for the SPH simulations.

### *2.3. Experimental and numerical test cases*

For all test cases, monochromatic (regular) waves are generated with frequency, $f_0 = 19/32 \approx 0.594$ Hz. The corresponding wavenumbers on the deeper ($k_{0d}$) and shallower ($k_{0s}$) sides are 1.85 m$^{-1}$ and $k_{0s} = 2.80$ m$^{-1}$, respectively. Hence, $k_{0d}h_d = 1.02$ and $k_{0s}h_s = 0.559$, and waves are in intermediate water depth both before and after the step.

Waves are generated for a range of amplitudes in both experiments and the numerical model, each for a duration of 30 s. In order to compare experimental and numerical wave parameters, measurements taken at gauge 1 from the experiments are initially assessed relative to equivalent measurements from the numerical model extracted at the same location ($x = -1.865$ m). The 'ramp-up' of the wave generation differs between the experimental and numerical wavemakers as does the sampling frequency. To remedy this, the wave gauge measurements are down-sampled to 20 Hz and, through cross-correlation analysis, the lag associated with the maximum cross-correlation value (measured at gauge 1 location) is removed from the start of all gauge measurements. This reduces both sets of measurements to a length of 29.15 s on a synchronised time base, $t$.

To enable assessment of the incident wave amplitudes in the numerical model and experiments, the mean wave amplitude measured at gauge 1 (or SPH equivalent) from $t = 17.9$ s to 29.15 s is used and referred to as $a_1$. This corresponds to the time window used for frequency-domain analysis in Section 3.1. These mean amplitudes will include reflections from the step and the effects of nonlinear waves, but enable fair comparison between the model and the experimental test cases.

The extracted experimental and numerical reference wave amplitudes $a_1$ are presented in

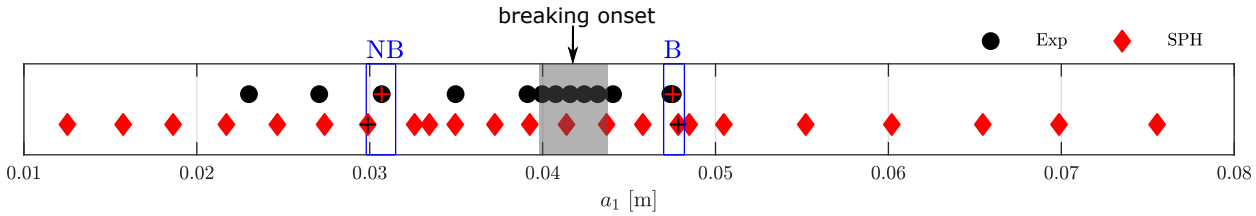


**Figure 3:** Mean amplitudes measured from experiments and the SPH model from 17.9 s to 29.15 s, showing breaking (B) and non-breaking (NB) cases used for direct comparison. The grey transparent patch denotes the region where breaking is observed (the left-hand side of the patch corresponds to where mild inconsistent breaking is observed and the right-hand side to where breaking became persistent).

Fig. 3. The high-density region of wave amplitudes for the experimental cases was used to identify the threshold amplitude(s) at which waves begin to break, which is highlighted by the grey transparent patch. The left-hand side of the patch defines the amplitude where breaking occurs infrequently, not for every crest and if so very gently, and the right hand-side corresponds to consistent breaking for consecutive waves. Very large amplitudes are generated in the SPH model to assess how breaking behaviour changes and limits shallower-side amplitudes. For direct comparison, a breaking (B) and a non-breaking case (NB) for which amplitudes are very similar are identified and are encircled by a blue box in Fig. 3. These cases are used for the convergence study (Section 2.4) and for more detailed comparisons and analysis throughout Section 3.1.

As will become apparent in Section 3.2, the values of $a_1$ are not exactly equal to the incident wave amplitude, as values of $a_1$ include reflections from the step. Due to the wave gauge placement (single gauge on the deeper-side), it was not possible to calculate the true incident amplitudes for the experiments. For the SPH simulations, however, the high-resolution surface elevation outputs facilitate reflection analysis to isolate the incident and reflected waves, the results of which are presented in Appendix A. Reflected wave amplitudes are found to be 22-28% of the incident wave amplitude. In Section 3, results are presented relative to $a_1$ when both SPH and experiments are included, and relative to the calculated value of the incident amplitude from SPH simulations, $a_{1,i}$, when only SPH results are presented.

### *2.4. Model convergence and example outputs*

In order to assess convergence and model performance, the initial particle spacing $d_p$ was varied for the breaking (B) and non-breaking (NB) validation cases. Particle spacing values of $d_p$ = 0.02 m, 0.01 m and 0.005 m were used. Fig. 4 shows the difference between wave gauge measurements and SPH measurements, represented by the coefficient of determination $r^2$ for both the breaking (B) and non-breaking (NB) cases and for three values of $d_p$. Values of the coefficient of determination $r^2$ are based on the second half of the time signal ($t$ = 17.9 s to 29.15 s) to ensure waves, including second-order free waves have reached all wave gauges. This window also corresponds to the section used for frequency-domain analysis in Section 3.1.

In general, decreasing $d_p$ serves to improve the comparison. Very good agreement is observed between the simulations and wave gauges near to the step for $d_p$ = 0.005 m; $r^2$-values between 0.98 and 0.995 are calculated for gauges 1–9 for both B and NB cases. Mean $r^2$-values over all gauges are approximately 0.96 and 0.93 for the non-breaking and breaking cases, respectively.

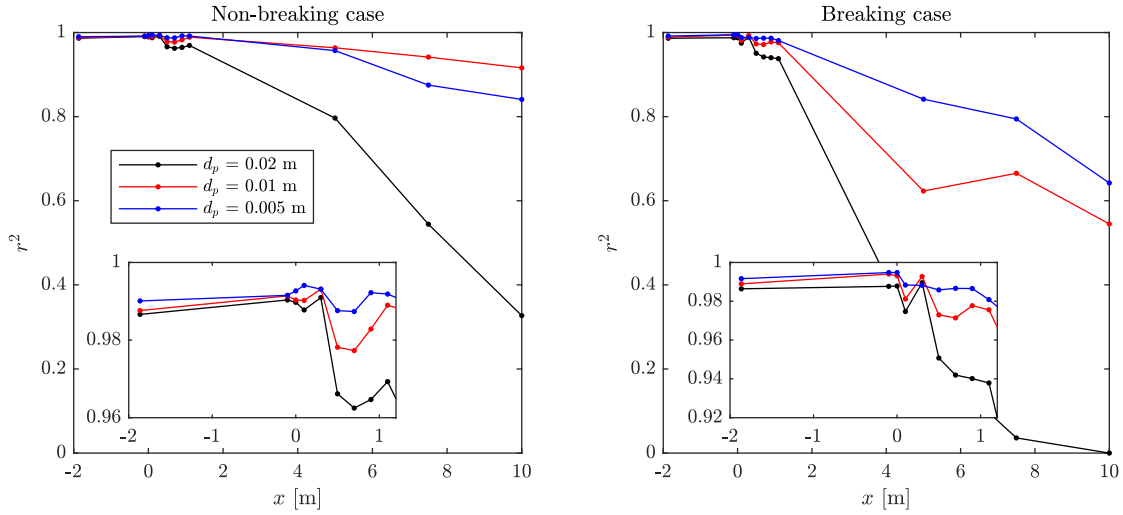


**Figure 4:** Coefficient of determination ($r^2$) between SPH model and experiments as a function of gauge position and for three values of the particle spacing $d_p$. Both non-breaking (NB, left) and breaking (B, right) cases are shown. The inserts within each plot show $r^2$-values in the region near to the step.

Although poorer performance is observed further from the wavemaker (and step), this is deemed as acceptable agreement, particularly considering the measured discrepancy in input amplitude as presented in Fig. 3. The increased discrepancy between the experimental and numerical surface elevations with increasing $x$ on the shallower side ($x > 0$) for the non-breaking case is likely due to the non-physical large artificial viscosity required to keep simulations stable along with the dissipative effects of the density diffusion scheme. For the breaking case, this, in combination with the three-dimensional and turbulent nature of the breaking itself, contributes to the discrepancy. As will become apparent, the surface elevations near to the step are of most interest, and in this region there is very good agreement. A value of $d_p = 0.005$ m was used for all subsequent simulations.

Detailed analysis in Sections 3.1 and 3.2.1 largely focuses on extracted superharmonics, and hence some example outputs of complete spatial and temporal measurements are shown in this section. Fig. 5a, b show the SPH particle velocities in the $x$-direction, $v_x$, for the breaking (B) case. Also presented are the interpolated surface elevations from the SPH simulations and the wave gauge measurements from experiments, between which good agreement is demonstrated. The aforementioned free second-order superharmonic is visible as are the associated large crest amplitudes near to the depth transition, prior to breaking. Wave breaking is subsequently apparent between gauges 9 and 10. Fig. 5c shows time series of surface elevations for the breaking case at gauge 9. Synchronisation, as mentioned in Section 2.3, is based on gauge 1 measurements. Gauge 9 is at a location where the free and bound second-order superharmonics are coming into phase; hence the surface elevation is highly asymmetric, and indeed the wave form indicates the presence of additional free components. The SPH model agrees well with the experimental measurements, although the difference in wavemaker 'ramp-up' is evident for the first measured wave.

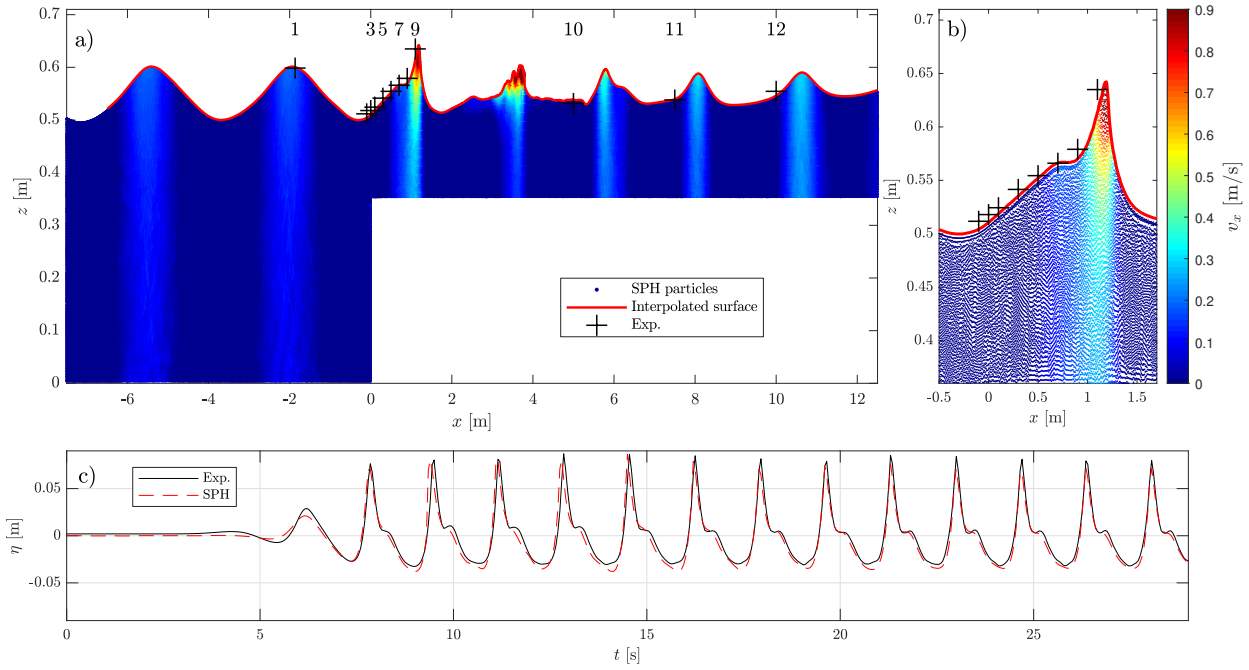


**Figure 5:** Panels a) and b) show particle velocities in the $x$-direction, $v_x$, along with interpolated free surfaces from SPH simulations and experiments at the gauge locations (Exp.) for the breaking case defined in Fig. 3 at a simulation time of 14.5 s. Panel c) shows a time-domain comparison between the SPH and experimental measurements at gauge 9 for the breaking case.

## 3. Results

### *3.1. Frequency and time-domain analysis*

This section assesses the release of wave harmonics due to nonlinear monochromatic waves transitioning over an ADT and validates the SPH model through comparisons of the extracted superharmonics from the SPH simulations to those from experimental observations.

To assess the superharmonics, Fast Fourier Transforms (FFTs) are used to extract harmonic amplitudes, and for all harmonic analysis, the synchronised time window between 17.9 s to 29.15 s is used (see Section 2.3) to ensure wave components have had time to travel across the measurement domain. This precise section length also minimises spectral leakage, enabling harmonics to be extracted readily from the FFTs. Fig. 6 shows amplitude spectra for several wave gauges for the non-breaking (NB, top row) and breaking (B, bottom row) cases. SPH equivalents are also shown.

Assessing the non-breaking (NB) case shown in Fig. 6, it is apparent that on the deeper side (gauge 1) the waves are only weakly non-linear, as the second superharmonic amplitude is over an order of magnitude smaller than the first harmonic and the third and fourth superharmonic waves are negligibly small. Compared to the deeper side (gauge 1), an increase in the amplitude of the second harmonic is shown at the step interface (gauge 3), whereas an increase in all superharmonic amplitudes is shown for all gauges further downstream from the step (gauges 5 to 9). At gauge 9, up to the sixth-harmonic component become notable. Further from the step, at gauge 10, all superharmonic amplitudes are reduced compared to those measured at gauge 9. Fig. 6 clearly

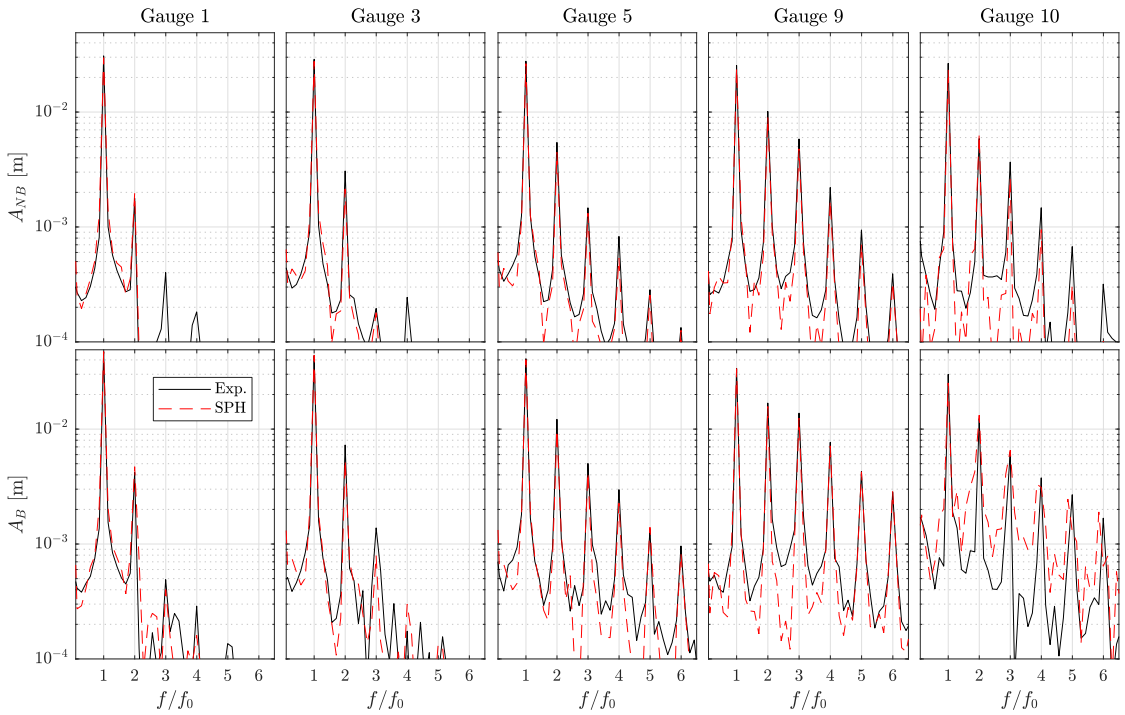


**Figure 6:** Discrete amplitude spectra of the surface elevations measured at the different gauge positions in the experiments compared to analogous spectra obtained from SPH simulations for breaking (B) and non-breaking (NB) cases.

indicates a spatially in-homogeneous wave field with a localised peak. This in-homogeneity is a result of the second-order effects that are investigated by [9, 17] and, in addition, their higher-order counterparts. Following Massel [9] and Li et al. [17], we know free waves with frequency $2f_0$ are released at the step, where $f_0$ denotes the incident linear wave frequency. The transmitted free wave obeys (approximately for waves of larger steepness) the linear dispersion relation

$$16\pi^2 f_0^2 = g k_{2f_0,s} \tanh k_{2f_0,s} h_s, \tag{10}$$

where $g$ is gravitational acceleration, and $k_{2f_0,s}$ denotes the wavenumber of the transmitted second-order superharmonic free wave on the shallower side. This free wave generally has a phase shift of $\varphi_{2s} \approx \pi$ relative to the second-order superharmonic bound wave that also exists in the absence of the step [17]. The superharmonic free and bound waves can be linearly superimposed, leading to a spatial beating pattern in the surface elevation, which reaches its first peak in the vicinity of gauge 9. Li et al. [17] suggests that the first peak location, $x_p$, measured from the step interface, appears in the region

$$\frac{0.9\pi}{k_{2f_0,s} - 2k_{0,s}} \lesssim x_p \lesssim \frac{1.1\pi}{k_{2f_0,s} - 2k_{0,s}}, \tag{11}$$

where $k_{0,s}$ denotes the wavenumber of the linear transmitted wave on the shallower side. The lower and upper limits, $0.9\pi$ and $1.1\pi$, were chosen in this paper as the phase shift, $\varphi_{2s}$, between the bound and free is not exactly $\pi$ and [9, 17] can only provide a leading-order estimate for the steep waves we consider here. For the case presented in this paper, $\varphi_{2s}$ is predicted to be $0.92\pi$ based on [9, 17]. Furthermore, the locations of the maximum (anti-node) and minimum crests (node) associated with the beating pattern can be estimated by $(\varphi_{2s} + (2n-2)\pi)/(k_{2f_0,s} - 2k_{0,s})$ and $(\varphi_{2s} + (2n-1)\pi)/(k_{2f_0,s} - 2k_{0,s})$, respectively, where $n$ is a positive integer and $0.9\pi \lesssim \varphi_{2s} \lesssim 1.1\pi$. These locations will be examined in §3.2, and we will show in §3.3 that the first anti-node location, $x_p$, is a good estimate of the location at which the waves start to break when the incident wave amplitude is gradually increased.

The spatial beating pattern of the second-order free and bound waves also appears to correlate with an increase in amplitude of higher harmonics (third to sixth). In Section 3.2.1 the higher harmonics are explored in more detail, before assessing how this influences breaking behaviour in Section 3.3. SPH measurements compare favourably to experiments for all gauges, however, minor deviation is noted for gauge 10, particularly for fourth and higher superharmonic amplitudes. This may be attributed to the aforementioned excessive dissipation in the SPH simulations, the effects of which accumulate downstream from the step and disproportionately affect the higher frequencies.

Similar results are evident for the breaking case (B), as shown in Fig. 6. Compared to the deeper side, superharmonic amplitudes increase up to gauge 9, then decrease for gauge 10. In this case, however, as shown in Fig. 5, the waves break between gauge 9 and 10. Again, good agreement is found between the SPH model outputs and experiments for gauges 1 to 9, with significantly poorer agreement for gauge 10. The wave breaking process, which results in energy dissipation and re-distribution, is imperfectly modelled, resulting in small errors in both the frequency and amplitude of higher-frequency components (at gauge 10, downstream of breaking).

To assess wave harmonics in the time domain, inverse Fourier Transforms applied to each isolated harmonic are computed, with the results for the breaking (B) and non-breaking (NB)

cases shown in Figs. 7 and 8. Harmonics are normalised by the deeper-side reference amplitudes, $a_1$, presented in Fig. 3. The increase in superharmonic amplitudes locally at gauge 9 is clearly significant and is captured well by the SPH model for both cases. The change in wave profile and amplification of the crest amplitude from gauge 1 to gauge 9 is quite striking, and the subsequent reduction in crest amplitude at gauge 10 highlights the localised nature of the phenomenon. As observed in Fig. 6, the SPH results at gauge 10 for the breaking case do not agree well with the experiments for the higher superharmonics (fifth and sixth).

Fig. 9 shows the amplitudes for the different harmonics, extracted from the spectra, as a function of $a_1$ for experiments and SPH simulations at several gauge positions. Results from all experimental cases are shown in addition to the SPH simulations up to $a_1 = 0.05$ m. From Fig. 9 it is evident that for all $a_1$ values shown the deeper-side incident wave fields remains weakly nonlinear with second-order contribution up to $0.1a_1$. Higher superharmonics become increasingly significant near to the step on the shallower side, where at gauge 9 even the contribution of the sixth superharmonic component becomes significant for larger amplitudes. The amplitudes of all superharmonics are reduced at gauge 10, where free and bound second-order components are no longer in phase, and after $a_1 \approx 0.04$ m it is clear that breaking is limiting the superharmonic amplitudes further. Overall, reasonable agreement is found between SPH simulations and experiments for all harmonics, input amplitudes and wave gauge positions. The notable disagreement found at second order for gauge 3 is perhaps expected as the gauge is located at the depth transition where any minor position error will result in large differences in the harmonic content. Disagreement at gauge 10 is more significant than at other gauges, and is more pronounced at higher values of $a_1$, which can be explained by the presence of wave breaking, which is three-dimensional, turbulent, and not perfectly modelled in the SPH simulations.

### *3.2. Spatial analysis*

In the SPH simulations the harmonics presented in the time domain in Figs. 7 and 8 can also be plotted as a function of space and compared to gauges at the measurement locations. Fig. 10 and Fig. 11 present this for the non-breaking and breaking cases, respectively. The synchronised time presented of $t = 17.9$ s ensures the free second-order superharmonic has had time to propagate to the end of the measurement domain. For both the non-breaking (Fig. 10) and breaking (Fig. 11) cases excellent agreement is found between experiments and SPH simulations for the phase-resolved harmonics. Assessing the second-order superharmonic in Figs. 10 and 11, the approximate node and anti-node locations, measured from the step interface, are seen near $x = 3$ m, 6 m, and 9 m. These locations agree well with the estimates from Eq. (11) and [9, 17] for the case considered: with $x_p \approx 2.86$ m using $k_{2f_0,s} = 6.67$ m$^{-1}$, $2k_{0,s} = 5.66$ m$^{-1}$, and the phase difference between free and bound second-order components at the step $\approx 0.92\pi$ based on [17]. For the apparent node at $x = 6$ m there is an almost perfect cancellation of the surface elevation at the time presented, which suggests that the free and bound waves are of very similar amplitude. At this node, the amplitudes of the higher harmonics are also significantly reduced. For the breaking case presented in Fig. 11, the first anti-node is clearly observed, with significantly larger superharmonic amplitudes than in the non-breaking (NB) case, however, a clear second anti-node is not observed after the breaking location.

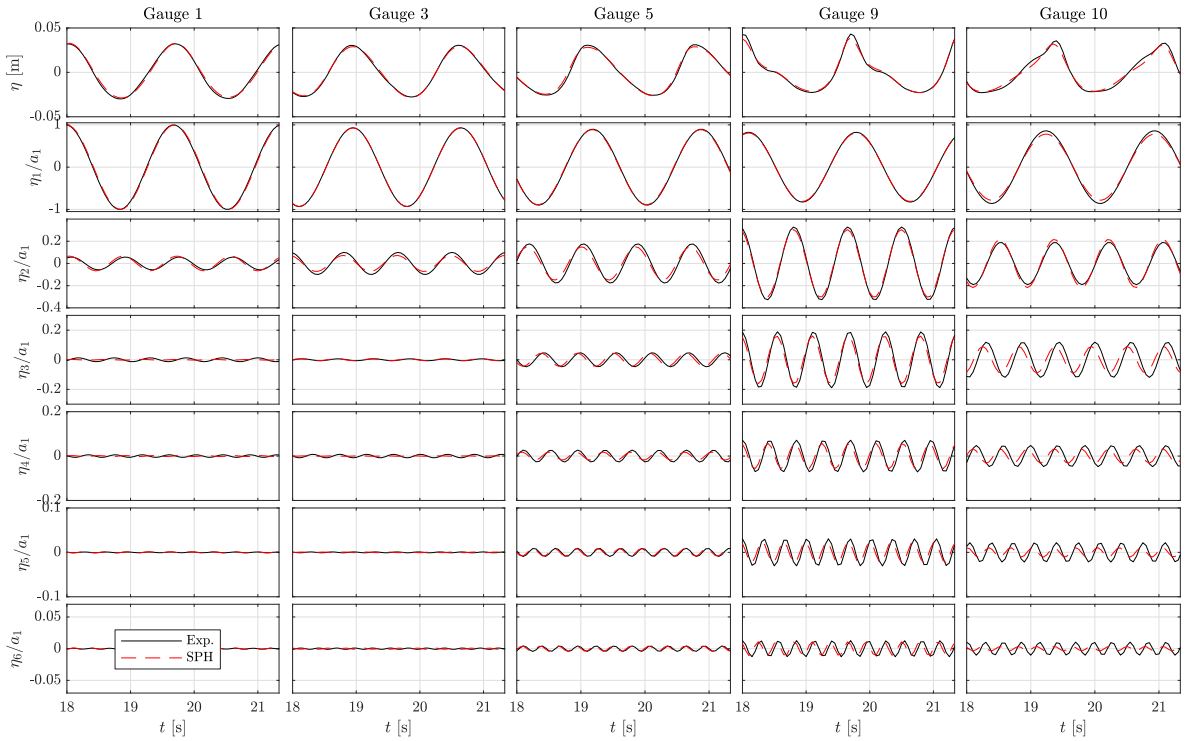


**Figure 7:** Comparison of separated harmonic time series for the non-breaking case showing experiments and SPH simulations for several gauge positions.

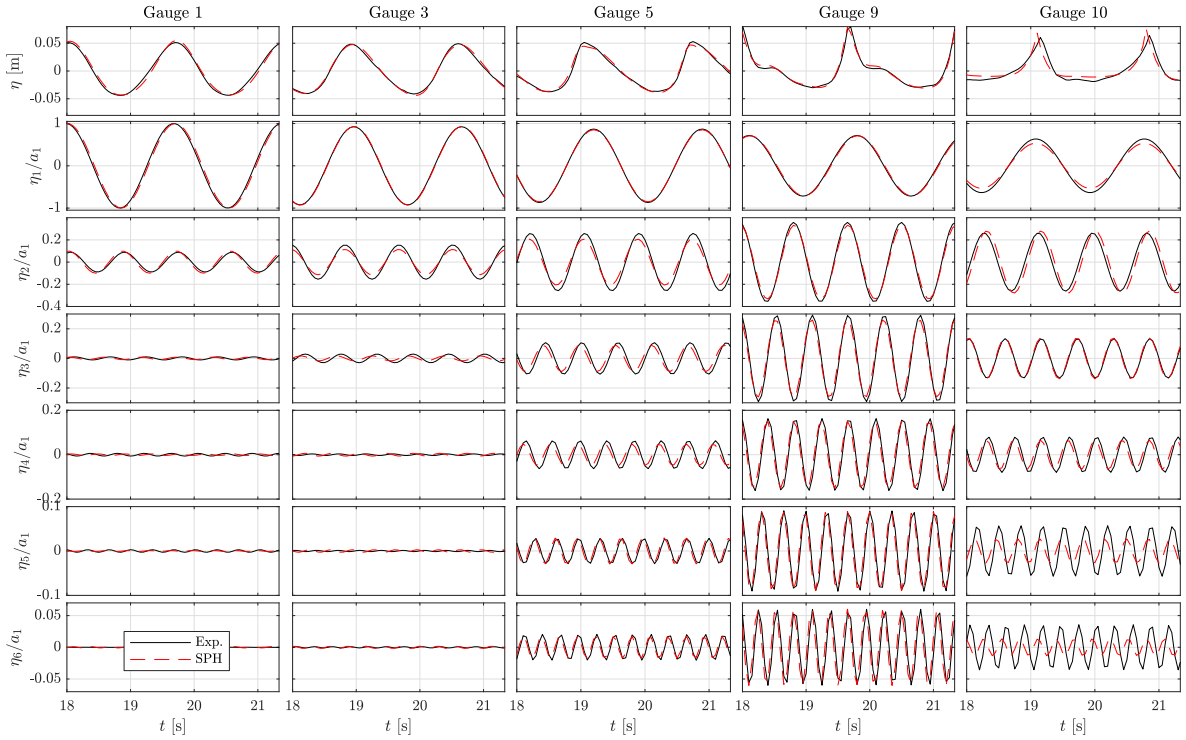


**Figure 8:** Comparison of separated harmonic time series for the breaking case showing experiments and SPH simulations for several gauge positions.

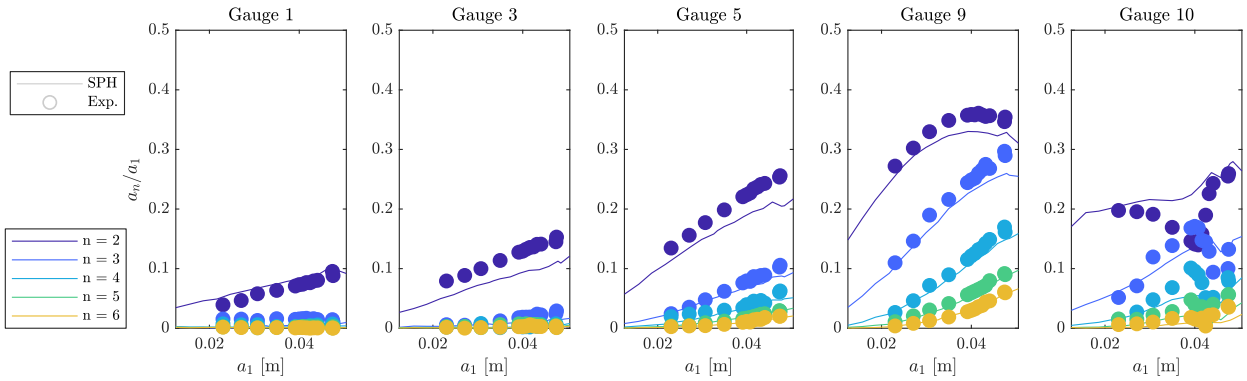


**Figure 9:** Extracted normalised higher-harmonic amplitudes $a_n/a_1$ at different gauge positions as a function of input amplitude $a_1$ comparing experiments and SPH simulations.

Fig. 12 presents the amplitudes associated with the first to the sixth harmonics as a function of space for four incident wave amplitudes including the breaking (B) and non-breaking (NB) cases, with both SPH simulations and experimental values shown in panels b–d. Also presented for panels a–c are the values expected from the second-order theory by Massel [9], as implemented in [17].

It is evident from Fig. 12 that the higher-harmonic components appear to have the same beating pattern as the second-order components. This suggests the origin of these components; i.e. the third and higher harmonics are bound to the second harmonic. If these were free components released at the ADT, one would expect higher-wavenumber beating patterns than those observed. For the lower amplitude cases (panels a–c) there is a clear second anti-node, which is not apparent in the breaking (B) case (panel d) as high-frequency surface motion is dissipated by breaking. On the shallower side, there is modulation of the amplitude of the first harmonic, which may be a result of third-order interaction, considering that the cross-interaction of the second-order free and transmitted linear would lead to a third-order bound wave of frequency $f_0$ but a wavenumber ($k_{2f_0,s} - 2k_{0,s} \approx 1$ m$^{-1}$) different from the wavenumber of the first harmonic. It is also noteworthy that amplitude of the second harmonic exceeds the amplitude of the first harmonic for the breaking (B) case at $x \approx 3$ m. For $x < 0$, there is a clear oscillation of the amplitude of the first harmonic due to the partial standing wave formed as a result of wave reflection from the step. It is evident that $a_1$ is, therefore, not a representation of the true incident amplitude as gauge 1 is located where the incident and reflected wave components are in phase. A further assessment of the incident and reflected waves are presented in Appendix A with transmitted waves assessed further in Section 3.2.1. It is also noteworthy that amplitude of the second harmonic exceeds the amplitude of the first harmonic for the breaking (B) case at $x \approx 3$ m.

A number of observations can be made when comparing the extracted spatial distribution of harmonics from the SPH model (solid lines) to those expected based on the theory by Massel (1983) [9] (dashed lines). On the deeper side, good agreement between theory and SPH simulations is found for the linear wave amplitude and the spatial standing wave pattern that arises due to reflections from the step. On the shallower side, both the predicted linear and second-order harmonic amplitudes from [9] are larger than those measured in experiments and extracted from

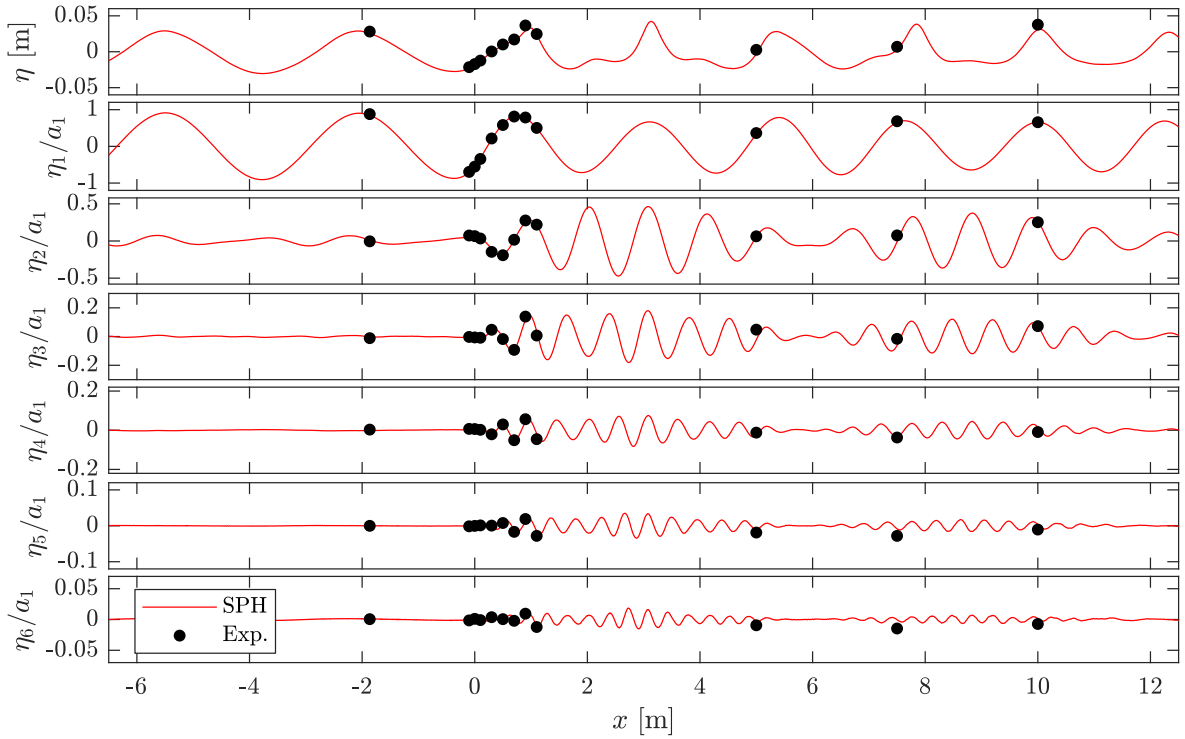


**Figure 10:** Separated harmonics from SPH simulations as a function of space and compared to experiments at the wave gauges for the non-breaking case at synchronised time $t$ = 17.9 s.

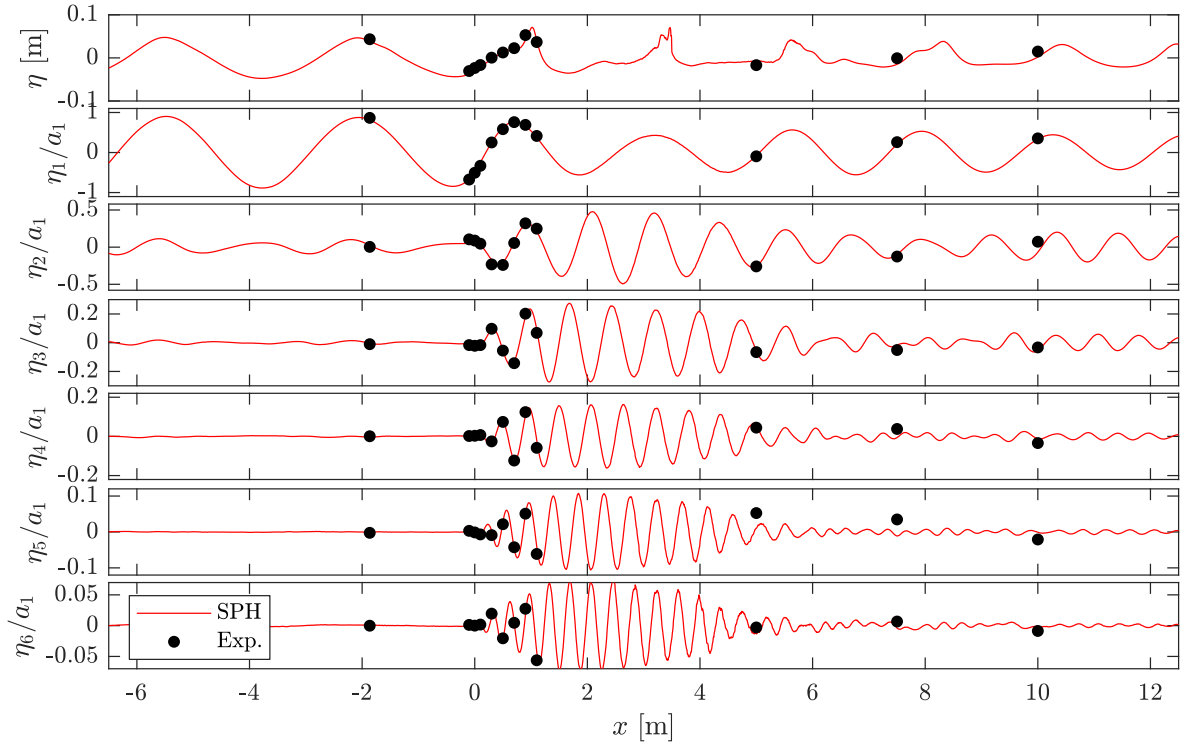


**Figure 11:** Separated harmonics from SPH simulations as a function of space and compared to experiments at the wave gauges for the breaking case at synchronised time $t$ = 17.9 s.

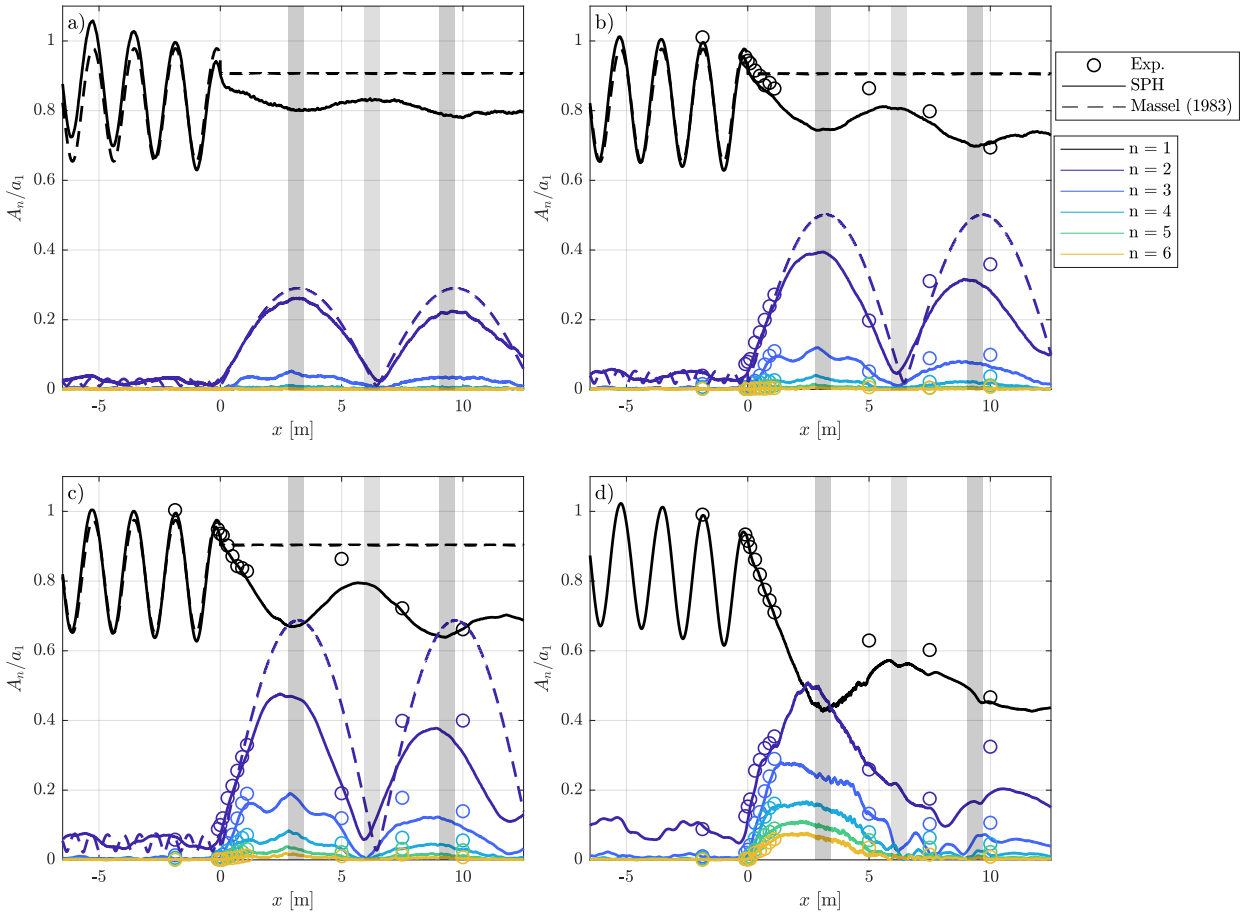


**Figure 12:** Spatial distribution of the amplitude of wave harmonics for select cases. a) $a_{1,i}$ = 0.0102 m, b) $a_{1,i}$ = 0.0177 m, c) non-breaking case $a_{1,i}$ = 0.0243, and d) breaking case $a_{1,i}$ = 0.0388 m. Experiments and SPH outputs are presented for cases b–d, along with second-order theoretical predictions by Massel (1983) [9] for the non-breaking cases (a–c). Transparent grey patches represent the expected node and anti-node locations.

the SPH model. This is due to the omission of higher-order effects in the theory, which would result in the forcing of higher modes. The predicted pattern of second-order beating, however, is consistent with the SPH simulations and experiments and is clearly the dominant mechanism at play. The near-perfect cancellation at $x \approx 6$ m arises because the theoretical bound and free second harmonic amplitudes are approximately equal, as also observed in the SPH simulations. The two lower-amplitude cases (panels a and b) demonstrate that, as the incident wave amplitude is decreased, the SPH simulations and experiments approach the second-order solutions of Massel [9]. Despite the omission of higher-order effects, it appears that the second-order beating effect described in [9, 17] can be used to predict where the maximum values of the surface elevation will be found. This is explored further in Section 3.3.

#### *3.2.1. Transmitted waves*

To better assess the harmonic content of the waves obtained from the SPH simulations upon transmission over the step, spatio-temporal ($k$-$f$) amplitude spectra have been computed for the total surface elevations on the shallower region over the synchronised time $t = 17.9$ s to 29.15 s. This enables the assessment of all present harmonic components, and is shown in Fig. 13 for four different cases. In Fig. 13 the linear dispersion relation is indicated by a blue dotted line, and a 1:1 relationship between $f/f_0$ and $k/k_{0s}$ is shown by a red dotted line, indicating a constant phase speed equal to that of the first harmonic and thus the location of bound waves. In Fig. 13, the amplitudes are normalised by the maximum value at the first harmonic and are compensated (scaled) by the ratio of $f/f_0$ to aid visual clarity of the (much smaller) higher-harmonic amplitudes on the colour scale. Due to the limited length of the shallower-side SPH domain (12.5 m), the wavenumber resolution is relatively coarse at $\Delta k = 0.503$ m$^{-1}$.

Despite the relatively coarse wavenumber resolution, several observations can be made assessing the $k$-$f$ spectra presented in Fig. 13. It is clearly seen that, as we increase the incident amplitude (moving from panels a to d and e to h), the higher harmonics become more visible, demonstrating an increased ratio of their amplitudes to the transmitted first harmonic amplitude. Both free and bound second harmonics are present, corresponding to non-zero amplitudes lying on the blue and red dashed lines, respectively. It is also evident that the higher harmonics (third to sixth) are not free waves but bound, as indicated by their coincidence with the red dotted lines. Fig. 13e–g show that for the non-breaking cases, the free and bound second harmonics are of similar amplitude, as also noted in Section 3.2 and predicted by Massel [9]. For the breaking case (d, h), the distinction between the free and bound wavenumbers of the second harmonic is less clear. As the spatio-temporal spectra are essentially averages over the spatial domain, the distinction between pre- and post-breaking frequency-wavenumber spectra is not evident. This distinction could be made more visible by reducing the domain length over which spectra are computed. However, this will reduce the wavenumber resolution too much to resolve the separate components.

### *3.3. Harmonic-induced wave breaking*

For suitably large incident waves, the second-order beating phenomenon and the coupled local increase in the magnitude of the higher harmonics previously discussed will lead to breaking, as examined further in this section.

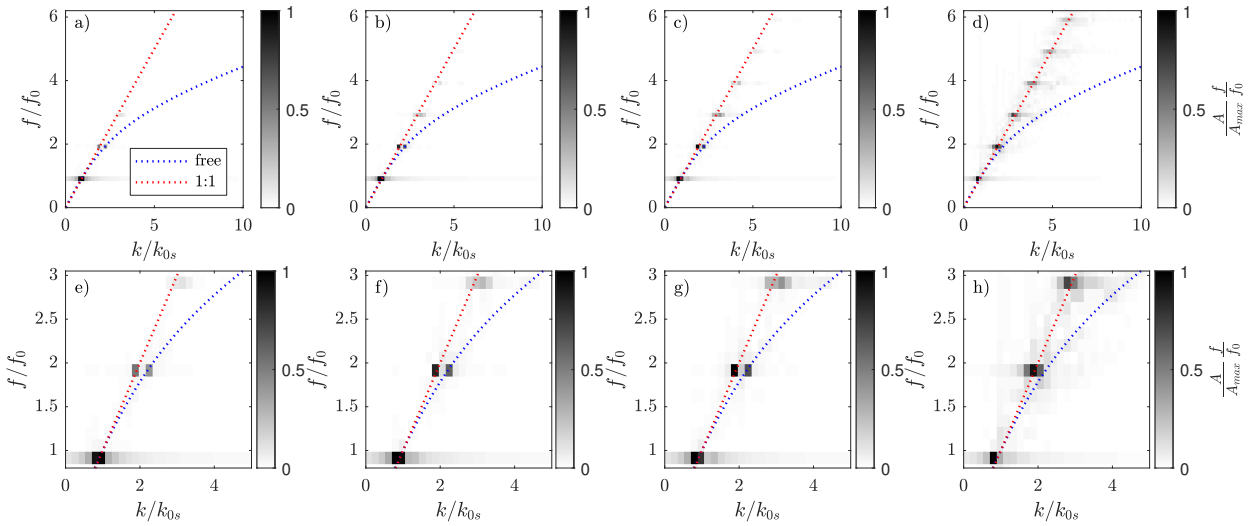


**Figure 13:** Spatio-temporal amplitude spectra for four cases with increasing amplitudes: a) $a_{1,i}$ = 0.0102 m, b) $a_{1,i}$ = 0.0177 m, c) $a_{1,i}$ = 0.0243 m (NB), d) $a_{1,i}$ = 0.0388 m (B). Panels e-h show zoomed-in regions for $f/f_0$ = 1–3 to assess second-order free wave content and correspond to panels a-d, respectively. Amplitudes have been scaled (compensated) by the ratio of $f/f_0$ to enable visualisation the higher-harmonic amplitudes, and are normalised by the maximum value at the first harmonic. Blue dotted lines denote the linear dispersion relation, and red dotted lines indicate a 1:1 relationship between $f/f_0$ and $k/k_{0s}$ and hence a constant phase speed equal to the phase speed of the first harmonic and thus the location of bound waves.

In Fig. 14, the wave evolution is shown for several wave amplitudes along with the corresponding velocity in the $x$-direction, $v_x$, for one instant in time. Increasing the wave amplitude (non-breaking cases), and hence the amplitude of the free and bound second-order waves (and higher-harmonic bound waves) serves to significantly alter the wave profiles and velocity. Crests become amplified and narrower; the effect of the free second-order harmonic on the surface elevation becomes clearly visible; amplitudes become more spatially variable, and velocities in the crest increase non-linearly with amplitude.

The $a_{1,i}$ = 0.032 m case ($a_1$ = 0.039 m) corresponds approximately to the lower breaking threshold identified in experiments (as shown in Fig. 3). For this case, the wave crest reaches over 2.5 times the incident wave amplitude before starting to spill over gently at around $x$ = 3 m, roughly at the location of the first anti-node ($x \approx 3.12$ m). As breaking is observed for this amplitude in the SPH simulations, this demonstrates that the SPH model appears to capture the breaking threshold well. For the $a_{1,i}$ = 0.039 m case (B, $a_1$ = 0.048 m), the wave crest also exceeds 2.5 times the incident wave amplitude, but this occurs much closer to the step before breaking more violently. As the wave amplitude increases, the breaking location moves nearer to the step, and for $a_{1,i}$ = 0.051 m occurs at $x \approx 1$ m. For this case, the normalised surface elevation ($\eta/a_{1,i}$) is greatly limited by breaking and does not significantly exceed 1.0.

To assess this harmonic-induced wave breaking further, we examine the maximum surface elevation as a function of the incident wave amplitude $a_{1,i}$ along with the locations of the maxima (as a proxy for breaking onset location, beyond the breaking threshold). This is presented in Fig. 15, along with the experimentally identified breaking onset thresholds highlighted in Fig. 3

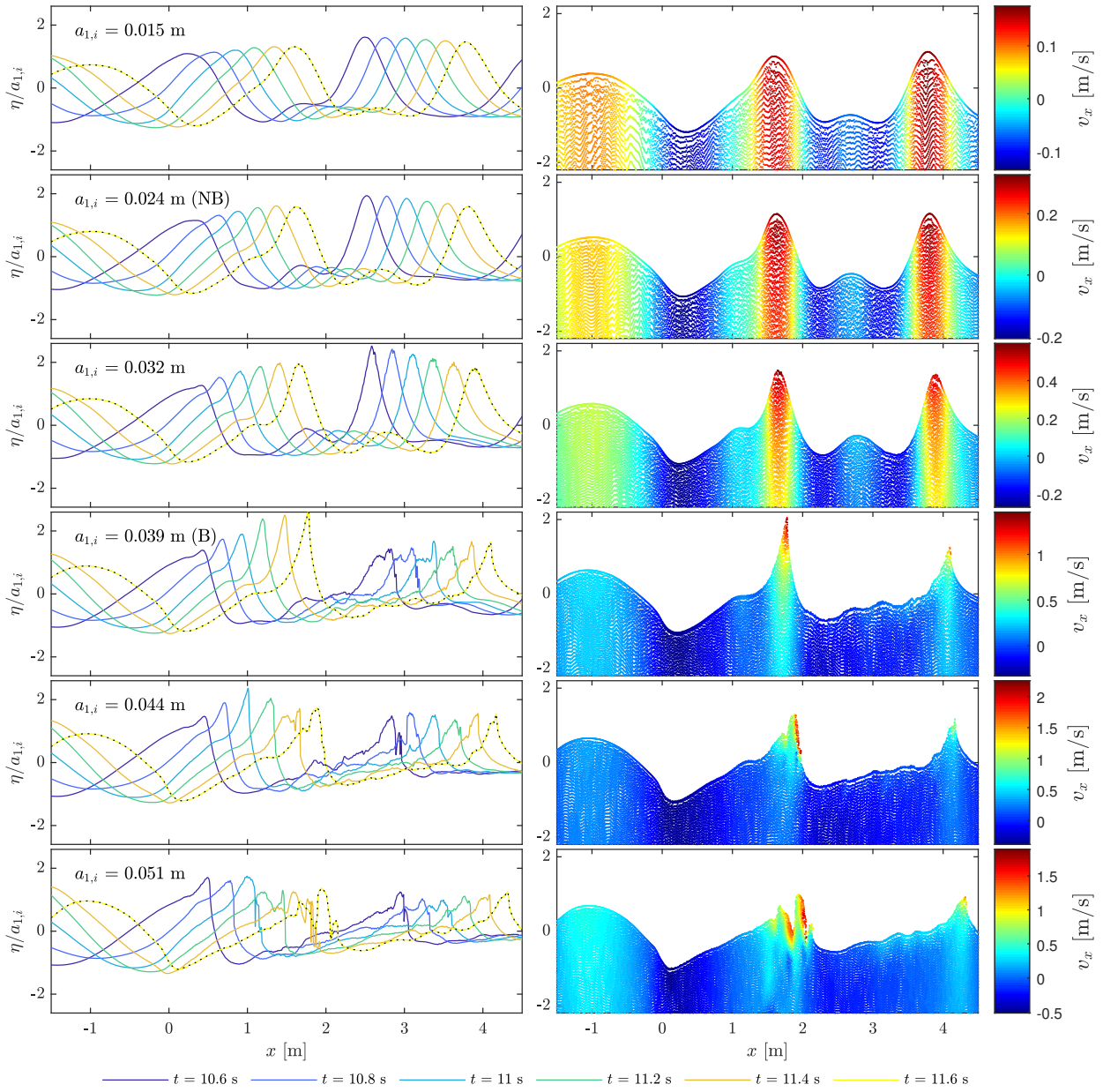


**Figure 14: Left:** evolution of surface elevation for different wave amplitudes (rows). **Right:** corresponding horizontal velocity fields for $t$ = 11.6 s (corresponding to the yellow and black dashed lines in the left-hand side panel). The second and fourth rows correspond to the NB and B cases, and the third corresponds to an input amplitude associated with the breaking limit.

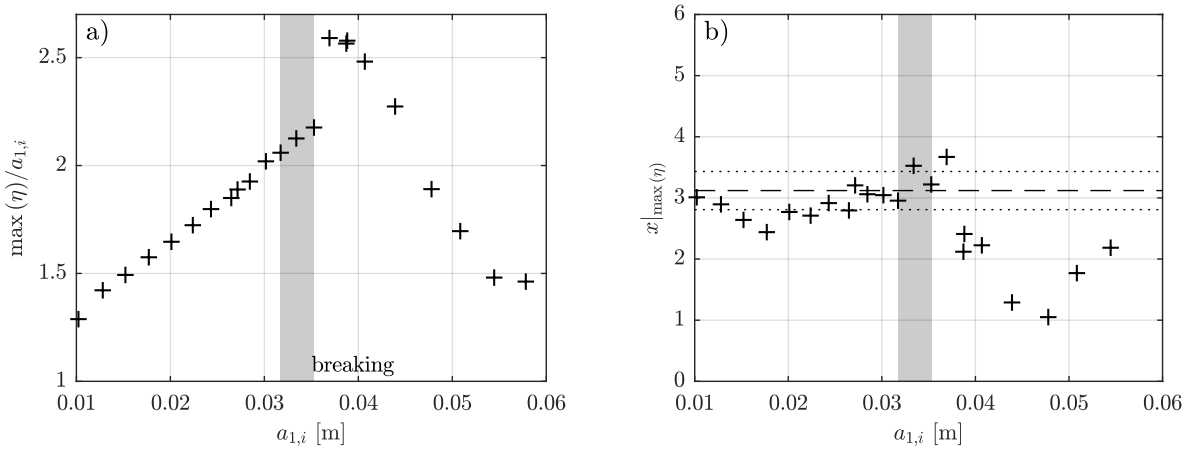


**Figure 15:** Panel a shows the maximum value of surface elevation normalised by incident amplitude as a function of incident amplitude. Panel b presents the corresponding locations of maximum surface elevation. The grey transparent area denotes the breaking threshold, and the dotted lines indicate the region $0.9\pi/(k_{2f_0,s} - 2k_{0,s})$ to $1.1\pi/(k_{2f_0,s} - 2k_{0,s})$.

(approximately converted to $a_{1,i}$ values). The dashed lines indicate the expected location of the first anti-node, $\pi/(k_{2f_0,s} - 2k_{0,s})$, with dotted lines bounding $0.9\pi/(k_{2f_0,s} - 2k_{0,s})$ to $1.1\pi/(k_{2f_0,s} - 2k_{0,s})$ as an ad-hoc estimation of the uncertainty of the true phase of the second-order free waves at the ADT for very steep-amplitude waves. Large values of the normalised surface elevation are calculated for values close to, and exceeding, the breaking amplitude threshold. The larger values of $\eta/a_{1,i}$ recorded just beyond the breaking threshold are likely due to jetting/spray. It is evident that the locations of the maxima agree well with the expected location of the first anti-node of the second-order beating pattern for amplitudes up to breaking, and hence define the expected breaking onset location for wave amplitudes at the breaking threshold. Past this threshold, the maximum value of the surface elevation occurs closer to the step (smaller $x$), as the combination of the first and higher harmonics even before the anti-node location increase the elevation to a value above the breaking limit.

Fig. 16 shows the amplitudes of the superharmonics at the locations of maximum surface elevation as a function of incident amplitude $a_{1,i}$. For values of $a_{1,i}$ below the breaking threshold, the normalised superharmonic amplitudes all increase with $a_{1,i}$. At the breaking threshold (grey patch) significant higher-harmonic contribution is observed and the location of the higher-harmonic maxima moves closer to the step. For incident amplitudes larger than the breaking threshold, the relative value of higher harmonics increase further with $a_{1,i}$ up to a limiting value after the breaking threshold (and prior to the anti-node location). Hence, for incident wave amplitudes slightly above the breaking limit, at the point of breaking there is increased higher-order contribution to the wave form. For waves with incident amplitudes much larger than the breaking threshold, however, the higher-order contribution decreases with amplitude. This is a result of waves breaking prior to the anti-node location (indicated by the location of maximum surface elevation in Fig. 15), where the harmonics are observed to be a maximum. Hence, somewhat counter-intuitively, the incident waves with the highest steepness are found to be significantly less non-linear at the point of breaking. The presence or lack of higher-harmonic contributions at the breaking onset will define the

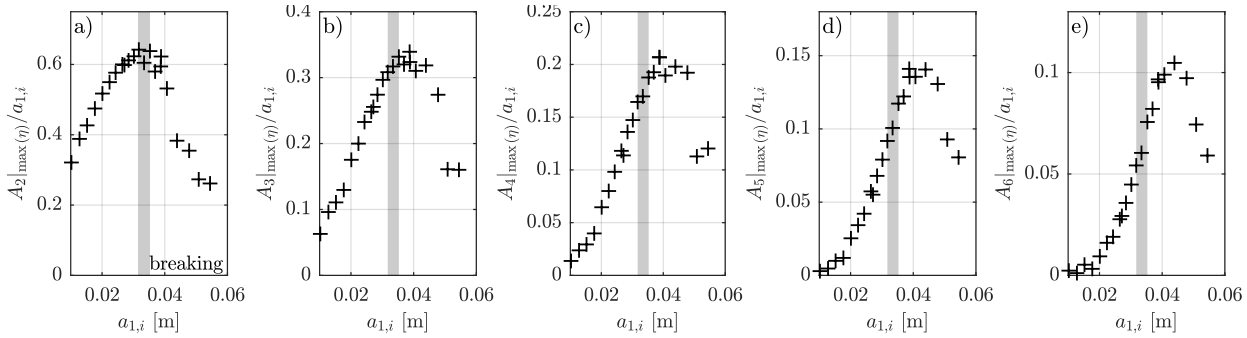


**Figure 16:** Values of normalised harmonic amplitudes at the location of maximum surface elevation (see Fig. 15) as a function of incident amplitude. Panels a) to f) correspond to values for the second to sixth harmonic, respectively. The grey transparent area denotes the breaking threshold.

kinematics and affect the resulting breaker characteristics.

## 4. Conclusions

In this paper we have experimentally and numerically assessed how harmonics generated at an abrupt depth transition (ADT) cause spatial variability of the wave field, and induce breaking on the shallower side of the ADT. The SPH model presented is found to agree well with experiments, and the high resolution of the model is used to explore the spatial distribution of harmonics and the onset of wave breaking.

From the SPH model results, we observe for the non-dimensional water depths considered that the higher harmonics (third to sixth) follow the spatial beating pattern of the free and bound second-order interaction predicted by [9] and are made up predominantly of bound components. We therefore conclude that these spatially variable bound higher harmonics fundamentally result from the second-order free-bound interaction. For incident wave amplitudes smaller than the breaking threshold, the locations of peak values of surface elevation, and the location where superharmonic amplitudes (second to sixth harmonic) are found to be at a maximum, are all predicted by this second-order beating phenomenon, despite significant higher-harmonic contributions to the wave fields. For incident wave amplitudes at the breaking threshold, breaking onset is also found to occur at this second-order anti-node location, whilst increasing amplitude above this limit serves to move the breaking onset location nearer to the ADT. The contribution of higher harmonics at the breaking onset is found to vary significantly depending on the breaking location: waves which have larger incident wave amplitudes break closer to the ADT and are associated with reduced higher-harmonic contribution. This observation has significant implications for the breaking wave kinematics and any associated loading on structures placed atop abrupt depth transitions.

For waves breaking due to ADTs, the breaking onset, location and associated kinematics are therefore dominated by the second-order free-bound interaction and associated local increase in the amplitude of higher harmonics. The breaking onset location beyond the breaking threshold is confined between the ADT ($x = 0$ m) and $x = \varphi_{2s}/(k_{2f_0,s} - 2k_{0,s})$, where $2k_{0,s}$ denotes the second-order superharmonic bound wavenumber, $k_{2f_0,s}$ the second-order superharmonic free wavenumber in the shallower depth, and $\varphi_{2s}$ is the free-wave phase shift which is approximately equal to $\pi$

(predicted to be $0.92\pi$ for the case presented based on second-order theory). Future work will extend this understanding to more realistic offshore scenarios, including multi-chromatic wave conditions and the effect of oblique angles of incidence and directional spreading.

## Acknowledgements

The experiments have been supported by NSFC-EPSRC-NERC Grants 51479114, EP/R007632/1, EP/R007519/1 and a Flexible Fund grant from UK China Centre for Offshore Renewable Energy. SD acknowledges the support from a Dame Kathleen Ollerenshaw Fellowship, YL from the Research Council of Norway through the FRIPRO mobility project 287389, and TSvdB from a Royal Academy of Engineering Research Fellowship. The authors would like to thank the members of the University of Plymouth COAST Laboratory for their help delivering the experiments, and would like to give a special thanks to Aaron English at the University of Manchester for their help with applying the modified dynamic boundary condition.

## References

[1] J. N. Newman, Propagation of water waves over an infinite step, J. Fluid Mech. 23 (1965) 399–415.
[2] J. T. Kirby, R. A. Dalrymple, Propagation of obliquely incident water waves over a trench, J. Fluid Mech. 133 (1983) 47–63.
[3] N. Booij, A note on the accuracy of the mild-slope equation, Coast. Eng. 7 (1983) 191–203.
[4] S. Beji, J. A. Battjes, Experimental investigation of wave propagation over a bar, Coast. Eng. 19 (1993) 151–162.
[5] Y. K. Zheng, Z. L. Lin, Y. Li, T. A. A. Adcock, Y. Li, T. S. van den Bremer, Fully nonlinear simulations of extreme waves provoked by strong depth transitions: the effect of slope, Phys. Rev. Fluids 5 (2020).
[6] K. A. Belibassakis, G. A. Athanassoulis, Extension of second-order Stokes theory to variable bathymetry, J. Fluid Mech. 464 (2002) 35–80.
[7] K. A. Belibassakis, G. A. Athanassoulis, A coupled-mode system with application to nonlinear water waves propagating in finite water depth and in variable bathymetry regions, Coast. Eng. 58 (2011) 337–350.
[8] R. Byrne, Field occurrences of induced multiple gravity waves, J. Geophys. Res. 74 (1969).
[9] S. R. Massel, Harmonic generation by waves propagating over a submerged step, Coast. Eng. 7 (1983) 357–380.
[10] I. R. Young, Wave transformation over coral reefs, J. Geophys. Res. 94 (1989) 9779–9789.
[11] H. Kojima, T. Ijima, A. Yoshida, Decomposition and interception of long waves by a submerged horizontal plate, Coastal Eng. (1991) 1228–1241.
[12] S. Beji, J. A. Battjes, Experimental investigation of wave propagation over a bar, Coast. Eng. 19 (1993) 151–162.
[13] K. Trulsen, H. M. Zeng, O. Gramstad, Laboratory evidence of freak waves provoked by non-uniform bathymetry, Phys. Fluids 24 (2012) 097101.
[14] K. Trulsen, A. Raustøl, S. Jorde, L. Bæverfjord Rye, Extreme wave statistics of long-crested irregular waves over a shoal, J. Fluid Mech. 882 (2020).
[15] J. D. Fenton, A fifth-order Stokes theory for steady waves, J. Waterw. Port C Div. 111 (1985) 216–234.
[16] E. Monsalve Gutiérrez, Experimental study of water waves: nonlinear effects and absorption, Ph.D. thesis, Université Pierre & Marie Curie-Paris 6, 2017.
[17] Y. Li, Y. Zheng, Z. Lin, T. A. A. Adcock, T. S. van den Bremer, Surface wavepackets subject to an abrupt depth change. part I: second-order theory, J. Fluid Mech. 915 (2021).
[18] Y. Li, S. Draycott, T. A. A. Adcock, T. S. van den Bremer, Surface wavepackets subject to an abrupt depth change. part II: experimental analysis, J. Fluid Mech. 915 (2021).
[19] Y. Li, S. Draycott, Y. Zheng, Z. Lin, T. A. A. Adcock, T. S. van den Bremer, Why rogue waves occur atop abrupt depth transitions, J. Fluid Mech. 919 (2021).
[20] O. Gramstad, H. Zeng, K. Trulsen, G. K. Pedersen, Freak waves in weakly nonlinear unidirectional wave trains over a sloping bottom in shallow water, Phys. Fluids 25 (2013) 122103.

[21] C. Viotti, F. Dias, Extreme waves induced by strong depth transitions: Fully nonlinear results, Phys. Fluids 26 (2014) 051705.
[22] G. Ducrozet, M. Gouin, Influence of varying bathymetry in rogue wave occurrence within unidirectional and directional sea-states, J. Ocean. Eng. Sci. 3 (2017) 309–324.
[23] J. Zhang, M. Benoit, O. Kimmoun, A. Chabchoub, H. C. Hsu, Statistics of extreme waves in coastal waters: Large scale experiments and advanced numerical simulations, Fluids 4 (2019) 1–24.
[24] C. T. Bolles, K. Speer, M. N. J. Moore, Anomalous wave statistics induced by abrupt depth change, Phys. Rev. Fluids 4 (2019) 011801.
[25] T. Ohyama, K. Nadaoka, Transformation of a nonlinear wave train passing over a submerged shelf without breaking, Coast. Eng. 24 (1994) 1–22.
[26] J. Grue, Nonlinear water waves at a submerged obstacle or bottom topography, J. Fluid Mech. 244 (1992) 455–476.
[27] J. Dattatri, H. Raman, N. Jothi Shankar, Performance characteristics of submerged breakwaters, Coast. Eng. (1978) 2153–2171.
[28] S. Beji, J. Battjes, Numerical simulation of nonlinear wave propagation over a bar, Coast. Eng. 23 (1994) 1–16.
[29] S. T. Grilli, J. Horrillo, S. Guignard, Fully nonlinear potential flow simulations of wave shoaling over slopes: Spilling breaker model and integral wave properties, Water Waves (2019) 1–35.
[30] M. A. Chella, H. Bihs, D. Myrhaug, Characteristics and profile asymmetry properties of waves breaking over an impermeable submerged reef, Coast. Eng. 100 (2015) 26–36.
[31] V. Srineash, K. Murali, Wave shoaling over a submerged ramp: An experimental and numerical study, J. Waterw. Port C Div. 144 (2018) 04017048.
[32] C. Altomare, J. M. Domínguez, A. Crespo, J. González-Cao, T. Suzuki, M. Gómez-Gesteira, P. Troch, Long-crested wave generation and absorption for SPH-based DualSPHysics model, Coast. Eng. 127 (2017) 37–54.
[33] S. J. Lind, R. Xu, P. K. Stansby, B. D. Rogers, Incompressible smoothed particle hydrodynamics for free-surface flows: A generalised diffusion-based algorithm for stability and validations for impulsive flows and propagating waves, Journal of Computational Physics 231 (2012) 1499–1523.
[34] M. Antuono, A. Colagrossi, S. Marrone, Numerical diffusive terms in weakly-compressible sph schemes, Computer Physics Communications 183 (2012) 2570–2580.
[35] Y. You, A. Khayyer, X. Zheng, H. Gotoh, Q. Ma, Enhancement of $\delta$-sph for ocean engineering applications through incorporation of a background mesh scheme, Applied Ocean Research 110 (2021) 102508.
[36] H. Gotoh, A. Khayyer, On the state-of-the-art of particle methods for coastal and ocean engineering, Coastal Engineering Journal 60 (2018) 79–103.
[37] A. J. Crespo, J. M. Domínguez, B. D. Rogers, M. Gómez-Gesteira, S. Longshaw, R. Canelas, R. Vacondio, A. Barreiro, O. García-Feal, Dualsphysics: Open-source parallel CFD solver based on smoothed particle hydrodynamics (SPH), Comp. Phys. Comms. 187 (2015) 204–216.
[38] J. M. Domínguez, G. Fourtakas, C. Altomare, R. B. Canelas, A. Tafuni, O. García-Feal, I. Martínez-Estévez, A. Mokos, R. Vacondio, A. J. Crespo, et al., DualSPHysics: from fluid dynamics to multiphysics problems, Comp. Particle Mech. (2021) 1–29.
[39] R. A. Dalrymple, B. Rogers, Numerical modeling of water waves with the sph method, Coast. Eng. 53 (2006) 141–147.
[40] A. Colagrossi, A meshless lagrangian method for free-surface and interface flows with fragmentation, These, Universita di Roma (2005).
[41] H. Gotoh, S. Shao, T. Memita, SPH-LES model for numerical investigation of wave interaction with partially immersed breakwater, Coast. Eng. J. 46 (2004) 39–63.
[42] H. Gotoh, Sub-particle-scale turbulence model for the mps method-lagrangian flow model for hydraulic engineering, Computational Fluid Dynamics Jour 9 (2001) 339–347.
[43] S. Shao, SPH simulation of solitary wave interaction with a curtain-type breakwater, J. Hydr. Res. 43 (2005) 366–375.
[44] X. Han, S. Dong, Interaction of solitary wave with submerged breakwater by smoothed particle hydrodynamics, Ocean Eng. 216 (2020) 108108.
[45] H. Akbari, M. Torabbeigi, Sph modeling of wave interaction with reshaped and non-reshaped berm breakwaters

with permeable layers, Applied Ocean Research 112 (2021) 102714.
[46] A. Khayyer, H. Gotoh, Y. Shimizu, K. Gotoh, H. Falahaty, S. Shao, Development of a projection-based sph method for numerical wave flume with porous media of variable porosity, Coastal Engineering 140 (2018) 1–22.
[47] N. Tsuruta, H. Gotoh, K. Suzuki, H. Ikari, K. Shimosako, Development of parisphere as the particle-based numerical wave flume for coastal engineering problems, Coastal Engineering Journal 61 (2019) 41–62.
[48] H. Wendland, Piecewise polynomial, positive definite and compactly supported radial functions of minimal degree, Adv. Comp. Math. 4 (1995) 389–396.
[49] G. Fourtakas, J. M. Dominguez, R. Vacondio, B. D. Rogers, Local uniform stencil (LUST) boundary condition for arbitrary 3-d boundaries in parallel smoothed particle hydrodynamics (SPH) models, Computers & Fluids 190 (2019) 346–361.
[50] T. Kanehira, H. Mutsuda, S. Draycott, N. Taniguchi, T. Nakashima, Y. Doi, D. Ingram, Numerical re-creation of multi-directional waves in a circular basin using a particle based method, Ocean Eng. 209 (2020) 107446.
[51] D. Molteni, A. Colagrossi, A simple procedure to improve the pressure evaluation in hydrodynamic context using the SPH, Comp. Phys. Comms. 180 (2009) 861–872.
[52] A. English, J. M. Dominguez, R. Vacondio, A. J. Crespo, P. K. Stansby, S. J. Lind, L. Chiapponi, M. Gomez-Gesteira, Modified dynamic boundary conditions (mDBC) for general purpose smoothed particle hydrodynamics (SPH): application to tank sloshing , dam break and fish pass problems, Comp. Particle Mech. (2021).
[53] O. S. Madsen, On the generation of long waves, J. Geophys. Res. 76 (1971) 8672–8683.
[54] J. Zelt, J. E. Skjelbreia, Estimating incident and reflected wave fields using an arbitrary number of wave gauges, in: Coast. Eng. 1992, 1993, pp. 777–789.
[55] S. Draycott, J. Steynor, T. Davey, D. M. Ingram, Isolating incident and reflected wave spectra in the presence of current, Coast. Eng. J. 60 (2018) 39–50.

## Appendix A. Incident and reflected waves

In Section 3.2 it was noted that the value of $a_1$ does not represent the linear incident amplitude. Hence, a simple frequency-domain reflection analysis was carried out on the SPH simulation data to identify the true incident amplitude. To separate the linear incident and reflected components, we use the approach detailed in [54] to resolve left and right-travelling wave components. This analysis is only carried out on the SPH simulation data, as having only a single gauge on the deeper side makes this analysis impossible for the experiments.

A subset of the SPH surface elevation data is used for analysis to avoid duplicate separations arising between measurement locations, and a target wave gauge array is defined based on a $12^{th}$-order Golomb ruler (similar to the approach implemented in [55]). Data is extracted at model-output locations closest to the target locations. The desired array, and co-array, defining the separations between all array locations, are presented in Figs. A.17 and A.18 (black circles) along with the locations used for analysis (red diamonds).

Fig. A.19 presents the outputs of the reflection analysis. Assessing Fig. A.19a, it is evident that the values of $a_1$ taken at gauge 1 are larger then the true incident amplitude ($a_{1,i}$) due to being at a constructive interference location. The reflection coefficient for the first harmonic (Fig. A.19b) is calculated to be between 0.22 and 0.28 and increases with incident amplitude. These values of $a_{1,i}$ are used to contextualise the breaking analysis presented in Section 3.3.

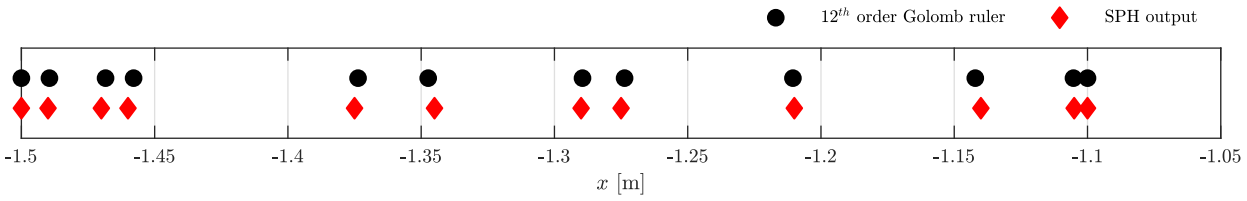


**Figure A.17:** Desired gauge spacing based on a $12^{th}$-order Golomb ruler along with SPH model output locations used for analysis.

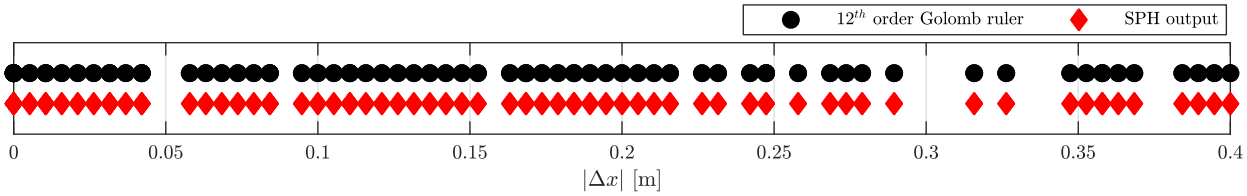


**Figure A.18:** Desired co-array separation based on a $12^{th}$-order Golomb ruler along with the obtained co-array using SPH model output locations.

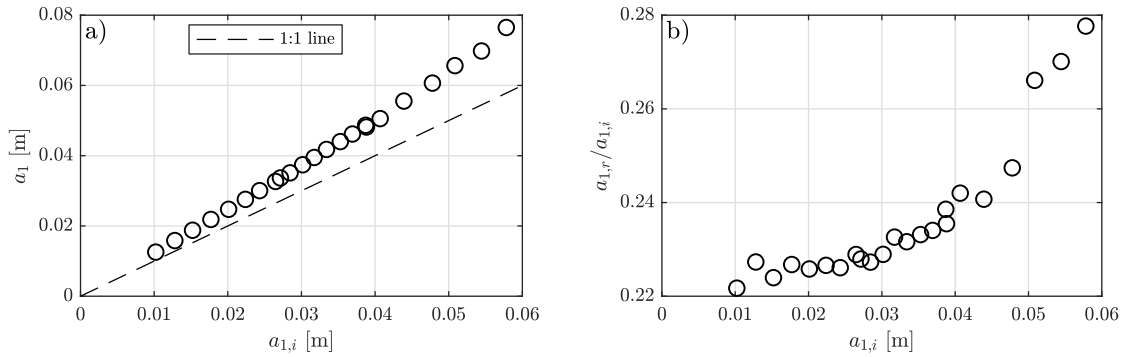


**Figure A.19:** Reflection analysis outputs for all SPH simulations. Panel a) shows the relationship between the reference amplitude $a_1$ and the true linear incident amplitude $a_{1,i}$. Panel b) presents the reflection coefficient as a function of the incident amplitude.